


Research Article

Pore-Scale Simulation of Water Flooding Using Volume of Fluid Method

Chuanqing Huang ¹, Jiaosheng Zhang,^{2,3} Xuejiao Lu,^{2,3} Li Jihong,^{2,3} Yingsong Huang,⁴ Lijie Liu,⁴ Yajie Su,⁵ and Jianguang Bai¹

¹College of Chemistry and Chemical Engineering, Shaanxi Key Laboratory of Chemical Additives for Industry, Shaanxi University of Science & Technology, Xi'an 710021, China

²Exploration and Development Research Institute, Changqing Oilfield Branch Company, PetroChina, Xi'an 710018, China

³National Engineering Laboratory for Exploration and Development of Low-Permeability Oil & Gas Fields, Xi'an 710018, China

⁴Research Institute of Exploration and Development, Shengli Oilfield Company, Sinopec Group, Dongying 257015, China

⁵Xigema Engineering Management Consulting Co., Ltd., Xi'an 710075, China

Correspondence should be addressed to Chuanqing Huang; huangcq@sust.edu.cn

Received 7 June 2022; Revised 9 November 2022; Accepted 24 November 2022; Published 17 February 2023

Academic Editor: Wenhui Li

Copyright © 2023 Chuanqing Huang et al. This is an open access article distributed under the Creative Commons Attribution License, which permits unrestricted use, distribution, and reproduction in any medium, provided the original work is properly cited.

Water flooding is a commonly used method in oilfield development, and the water flooding process is essentially the process of oil-water movement in porous media. Pore-scale flow law in water flooding process can guide the oilfield development plan, to improve the oil recovery efficiency. In this paper, the computational domain is constructed from the CT scan images of real cores. The oil-water flow process of the water flooding in the pore structure is simulated using the interFoam solver in OpenFOAM. The influence of the displacement process and the distribution of the remaining oil is analyzed in three aspects: the water cut curve, the state of the same water injection amount, and the final displacement state. The flow rate velocity affects the water flooding swept range, and the recovery factor increases gradually with the increase of the flow rate. With different injection velocity, the sweeping sequence of pores is different, and the location and shape of remaining oil are very different. Due to the different dominant forces under different wettability states, the swept patterns of the core are also different.

1. Introduction

At present, most of China's continental oilfields have entered a period of high water cut or even ultrahigh water cut. Two-thirds of the oil reserves remain in the underground oil layers and cannot be exploited [1–3]. In the middle and late stage of oilfield development, water injection is generally used. Experiments and data show that even in the high water cut stage, there are still original oil areas in the oil layer that have not been swept by water, and the residual oil saturation is about 50%, which has great potential for production in depth. The occurrence form and distribution characteristics of the remaining oil in the high water-cut stage are closely related to the pore properties of the reservoir. The changes of microscopic forces such as capillary

force have a particularly significant impact on the movement process of the remaining oil [4]. Therefore, how to improve the oil displacement efficiency in the high water cut stage has become the focus of industry research.

There are two methods to study pore-scale water flooding: microscopic physical experiment [5–9] and numerical simulation [10–13]. Microscopic physical experiments can capture the overall displacement law of the core and obtain the pore-scale flow behaviors. It has been extensively used in the investigation of the multiphase flow behaviors in enhancing oil recovery [14–16]. However, it is difficult for this method to accurately measure the internal displacement law of the core, especially the change and action mechanism of the microscopic force. In the numerical simulation of pore-scale two-phase flow, due to the existence of surface tension at the

two-phase interface, accurate calculation of the interface surface tension is the guarantee for calculating the microscale two-phase flow. Tracking the oil-water interface accurately is essential to capture oil-water phase behaviors. Generally, three different methods, front-tracking method (FTM) [17], level set method (LSM) [18], and volume of fluid (VOF) method [19], can be generally used. In FTM, the oil-water interface is represented by a surface mesh. The movement of the interface is realized by the movement of the grid points of the surface mesh. With this method, the surface tension can be accurately calculated. However, it is difficult for this method to treat complex topological change of the oil-water interface. As a result, this method is not suitable for tracking the oil-water interface in the complex porous media. In LSM, the oil-water interface is represented by the distance function to the oil-water interface, and complex topological change of the oil-water interface can be easily treated by this method. However, distance function does not have the information of the volume fraction, and the phase is not conserved. In VOF, the oil-water interface is represented by the phase volume fraction, and the volume is kept conserved during the calculation process, and the interface motion can be accurately tracked by using a high-precision solution algorithm or an accurate interface reconstruction technology. This method has been extensively used in the pore-scale simulation multiphase flow [10–13, 20, 21].

There are many previous studies on flow behaviors in water flooding process, and very valuable pore scale flow characteristics and phenomena have been obtained. However, there are few studies on oil-water distribution evolution and water flooding characteristics remaining oil distribution in different oil-water development cycles through numerical simulation technology under different injection rates and wettability. In this paper, the two-phase interfacial flow solver *interFoam* in OpenFOAM [22] is employed to track the oil-water flow. In this paper, the two-phase interfacial flow solver *interFoam* in OpenFOAM [22] is employed to track the oil-water flow. The *interFoam* solver uses Navier-Stokes equation to describe the oil-water motion and VOF method to represent the phase distribution. This solver has been validated in the work [23] and has been used in the simulation of pore-scale multiphase flow [24, 25], successfully. In the work, a physical model reconstructed from CT image of the sand stone, and numerical simulation of oil-water flow in the pore-space under different flow rate and different wettability is performed, and the characteristic of the remaining oil is also derived. The work is arranged as follows: the mathematical model is given in Section 2; the physical model, numerical condition, and boundary condition are given in Section 3; results and discussions are given in Section 4; and conclusions are given in the final section.

2. Mathematical Model

2.1. Continuity Equation.

$$\nabla \cdot \mathbf{u} = 0, \quad (1)$$

where \mathbf{u} is the velocity of water or oil.

2.2. Momentum Equation. In this work, Navier-Stokes equation is used to describe the oil-water motion.

$$\frac{\partial \rho \mathbf{u}}{\partial t} + \nabla \cdot (\rho \mathbf{u} \mathbf{u}) - \nabla \cdot (\mu \boldsymbol{\tau}) = -\nabla p + \rho \mathbf{g} + \sigma k \delta_s \mathbf{n}, \quad (2)$$

where t is time, p is pressure, \mathbf{g} is gravity acceleration, σ is surface tension coefficient, k is the interface curvature, δ_s is interface area per volume, and \mathbf{n} is interface normal. ρ is the average density, given by

$$\rho = \alpha \rho_w + (1 - \alpha) \rho_o. \quad (3)$$

ρ_w and ρ_o are density of water and oil, respectively. α is water volume fraction. μ is the average dynamic viscosity, given by

$$\mu = \alpha \mu_w + (1 - \alpha) \mu_o. \quad (4)$$

μ_w and μ_o are the dynamic viscosity of water and oil, respectively.

2.3. Volume Fraction Equation. In this paper, the VOF method is used to track the oil-water interface. This method uses the volume fraction α to represent the phase. When it equals to 1, the cell is occupied by water. When it equals to 0, the cell is occupied by oil; when it is between 0 and 1, the cell contains the oil-water interface.

$$\frac{\partial \alpha}{\partial t} + \nabla \cdot (\alpha \mathbf{u}) = 0, \quad (5)$$

where α is the water volume fraction.

3. Physical Model, Physical Boundary, and Numerical Boundary

The physical model used in this work is the computed tomography (CT) image of a sand stone, which is shown in Figure 1. The physical model is from Member 3 of Sha He Jie formation, Gudao Shengli Oil Field, China. The porosity of the porous medium is 0.29. In this image, black denotes pore channels, and white denotes stones. Because the shape of the pore throat channel is irregular and the structure is complex, a triangular mesh is used. The mesh includes 340124 elements, in the channels with smallest pore radius having about 20 mesh elements in radial direction, which is dense enough for oil-water flow in the porous media. In the meanwhile, we have also conducted the grid independence with 170450 mesh elements, 340124 mesh elements, and 652135 elements. It is found that the final oil-water distributions in the case with 340124 elements and the case with 652135 elements are almost the same. In order to lower the computational expense, the mesh with 340124 is employed in the later numerical tests. The model is a two-dimensional core structure with a length of 1 mm and a width of 0.9 mm. Gravity acceleration is not considered in the simulation.

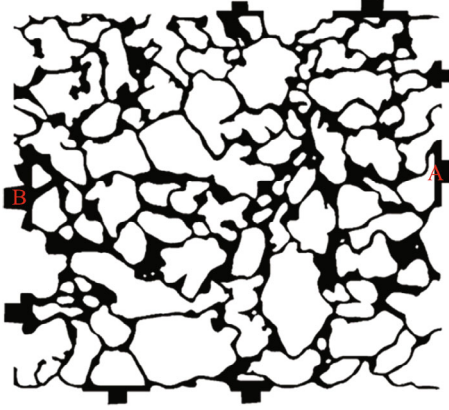


FIGURE 1: Pore geometry.

The porous medium is filled with oil initially. A is the inlet and B is the outlet; other boundaries are walls. The boundary conditions used in the simulation are given in Table 1. We use Neumann boundary condition for pressure at the inlet and wall and for the velocity and water volume fraction at the outlet. We use Dirichlet boundary condition for velocity at the inlet and wall and water volume fraction at the inlet, for pressure at the outlet. The physical properties of fluid used in the simulation are shown in Table 2. In order to investigate the injection velocity and wettability on the oil-water flow, we performed 25 test cases in this work. The injection velocities and contact angles in the tests are given in Table 3.

4. Results and Discussion

4.1. Effect of Flooding Velocity on the Oil-Water Flow. In order to investigate the effect of the injection velocity on the water flooding process, five different groups, 1-5, 6-10, 11-15, 15-20, and 20-25, were set in the simulation. Each group had the same contact angle, which was used to simulate five different states of wettability, i.e., strong water-wet, weak water-wet, neutral-wet, weak oil-wet, and strong oil-wet.

4.1.1. Water Flooding Curve. Figure 2 shows the water flooding curve with different injection velocities at different contact angles: (a) $\theta = 25^\circ$ (strong water-wet); (b) $\theta = 165^\circ$ (strong oil-wet). It can be seen that under the same wettability conditions, the higher the injection velocity, the higher the final water saturation, that is, the higher the oil recovery efficiency. And under the same wettability conditions, the water breakthrough time is basically the same. As shown in Figure 2(a), when the water saturation is about 0.32, there is water at the outlet. The velocity has little effect on the water-free oil recovery period. As can be seen from Figure 3(b), in the oil-wet state, the final water saturation at the velocity $u = 0.25 \text{ m} \cdot \text{s}^{-1}$ is higher than the water saturation at $u = 0.30 \text{ m} \cdot \text{s}^{-1}$. Therefore, it can be inferred that when the displacement velocity is higher than a certain value, the increase of the displacement velocity will lead to the decrease of the oil displacement efficiency. In the strong

TABLE 1: Boundary conditions.

Variables	Inlet	Outlet	Wall
p	Neumann	Dirichlet	Neumann
u	Dirichlet	Neumann	Dirichlet
α	Dirichlet	Neumann	contactAngle

oil-wet rock, the water flooding process is a typical drainage displacement, in which water is the nonwetting phase and oil is the wetting phase. As the increase of the flow rate, the drainage displacement pattern of water exhibits a transition from capillary fingering to viscous fingering, resulting in a decrease of water saturation [26]. In viscous fingering, the thin fingers followed a number of preferential flow path in the same direction as the injection and no backward movement. Therefore, it can be inferred that when the displacement velocity is higher than a certain value, the increase of the displacement velocity will lead to the decrease of the oil displacement efficiency. This can be explained as follows: in the strong oil-wet rock, the water flooding process is a typical drainage displacement, in which water is the nonwetting phase and oil is the wetting phase. As the increase of the flow rate, the drainage displacement pattern of water exhibits a transition from capillary fingering to viscous fingering, resulting in a decrease of water saturation [26]. In viscous fingering, the thin fingers followed a number of preferential flow path in the same direction as the injection and no backward movement. Therefore, it can be inferred that when the displacement velocity is higher than a certain value, the increase of the displacement velocity will lead to the decrease of the oil displacement efficiency.

4.1.2. Oil-Water Distribution with Same Injection Volume under Different Injection Velocity. Figures 4(a)–4(d) show oil distribution with same injection volume under different injection velocity ($0.10 \text{ m} \cdot \text{s}^{-1}$, $0.15 \text{ m} \cdot \text{s}^{-1}$, $0.20 \text{ m} \cdot \text{s}^{-1}$, and $0.25 \text{ m} \cdot \text{s}^{-1}$) under the water-wet condition (contact angle $\theta = 25^\circ$) before water breakthrough. In the figure, black represents oil, and gray represents water. It can be seen from the figure that, in general, there is little difference in the vertical and horizontal swept of different injection velocity, but there are some differences in the channels swept among different injection velocity. Under low-velocity conditions, the effect of fluid capillary action on the flow is relatively strong, which makes some channels with small pore radius more easily broken through in low-velocity conditions. The channel at point E in Figure 4(a), which is broken through at an inlet velocity of $0.10 \text{ m} \cdot \text{s}^{-1}$, but not at other higher velocities. The high pressure gradient created by the high injection velocity makes it easier for the fluid to break through in the direction of the shortest path. The fluid cannot pass through the channel where point A is located in Figure 4(a) at low speed, but can break through the channel at high speed, as shown in Figures 4(b)–4(d). Conversely, for channel B, which is parallel to the channel at point A, the fluid breaks through at low speed, but does not break through at high speed. From the different behaviors of the two channels A and B at different velocities in Figure 4(a),

TABLE 2: Physical properties of fluid.

Density of water $\text{Kg} \cdot \text{m}^{-3}$	Density of oil $\text{Kg} \cdot \text{m}^{-3}$	Kinematic viscosity of water $\text{m}^2 \cdot \text{s}^{-1}$	Kinematic viscosity of oil $\text{m}^2 \cdot \text{s}^{-1}$
1000	800	1×10^{-6}	1.89×10^{-5}

TABLE 3: Injection velocity and wall condition in different cases.

Case number	Injection velocity/ $\text{m} \cdot \text{s}^{-1}$	Contact angle/ $^\circ$
1	0.10	25
2	0.15	25
3	0.20	25
4	0.25	25
5	0.30	25
6	0.10	45
7	0.15	45
8	0.20	45
9	0.25	45
10	0.30	45
11	0.10	90
12	0.15	90
13	0.20	90
14	0.25	90
15	0.30	90
16	0.10	125
17	0.15	125
18	0.20	125
19	0.25	125
20	0.30	125
21	0.10	165
22	0.15	165
23	0.20	165
24	0.25	165
25	0.30	165

it can be found that under the condition of high-speed flooding in the hydrophilic environment, the fluid first selects the large-pore channel to flow and then flows from the large-pore channel into the small channels, as shown at point A in Figure 4(b). Under low-velocity conditions, the fluid first chooses small pore channels and then flows from small pore channels into large pore channels, as shown by point B in Figure 4(a). In the ultrahigh-speed environment, small pores and large pores may be simultaneously broken through, eventually resulting in the retention of oil in some channels perpendicular to the flow direction, similar to the position D in Figure 4(d). This phenomenon occurs in an oil-wet environment more common.

Figure 5 shows the distribution of oil and water at a certain time point before the outlet breaks into water under the same water injection volume and different water injection rates under oil-wet conditions. In the figure, black represents oil, and gray represents water. It can be seen from the figure that when the water injection volume is the same, the water

injection velocity has little effect on the sweep. In general, with the increase of injection speed, the viscous finger in the flow direction is slightly larger at low speed than that at high speed, and the flow perpendicular to the flow direction is slightly larger at high speed than at low speed. This is mainly because in the process of high-speed water flooding, the pressure difference between the inlet and the outlet is large, and the pressure field formed in the space is enough for the fluid to break through and enter the small pores, thereby achieving a larger sweep. As a result, more swept regions appear with high injection velocity than with low injection velocity.

4.1.3. Residual Oil Distribution under Different Injection Velocity. Figure 3 shows the final oil-water distribution at different water injection velocity under water-wet conditions. In the figure, black represents oil, and gray represents water. It can be seen from the figure that under the condition of low injection velocity, the spatial swept of water is small, and the residual oil in the swept area is mainly between the pores (point DEF in Figure 3(a)) and at the blind end. For instance, at point G in Figure 3(a), the swept area is large under high-speed conditions, and the remaining oil in the swept area mainly exists in the blind end, as shown at the point ABC in Figure 3(d). With low-speed water injection velocity, discrete water exists in the oil region of the swept boundary (point ABC in Figure 3(a)), which is caused by the capillary force, and the continuous water flow will protrude along the thin tube to form. The water flow is blocked, allowing water to enter the oil area, forming discrete water retention in the oil area. Under high-speed conditions, this part of the area is swept, and discrete water will be replaced by continuous water. Under water-wet conditions, there is basically no residual oil in the throat of the swept zone.

Figure 6 shows the final oil-water distribution at different water injection velocity under the oil-wet conditions. In the figure, black represents oil, and gray represents water. It can be seen from the figure that with the increase of water injection velocity, the spatial sweep is obviously enhanced. Whether at low speed or high speed, the remaining oil in the swept area is mainly in the state of oil-in-water (Figure 6(a) point ABCD), residual oil in the throat between pores (Figure 6(a) point E), residual at the blind end (point F in Figure 6(a)), and the film-like residual oil in the pores (points A and B in Figure 6(c)). With the increase of the injection velocity, the residual oil in the oil-in-water state and the residual oil in the interpore throat decreased significantly. For example, the oil-in-water residual oil at point B in Figure 6(a) and the residual oil in the throat at point E do not exist under high-speed injection velocity (the positions corresponding to Figures 6(c) and 6(d)). However, the residual film-like oil will increase at high speed. For

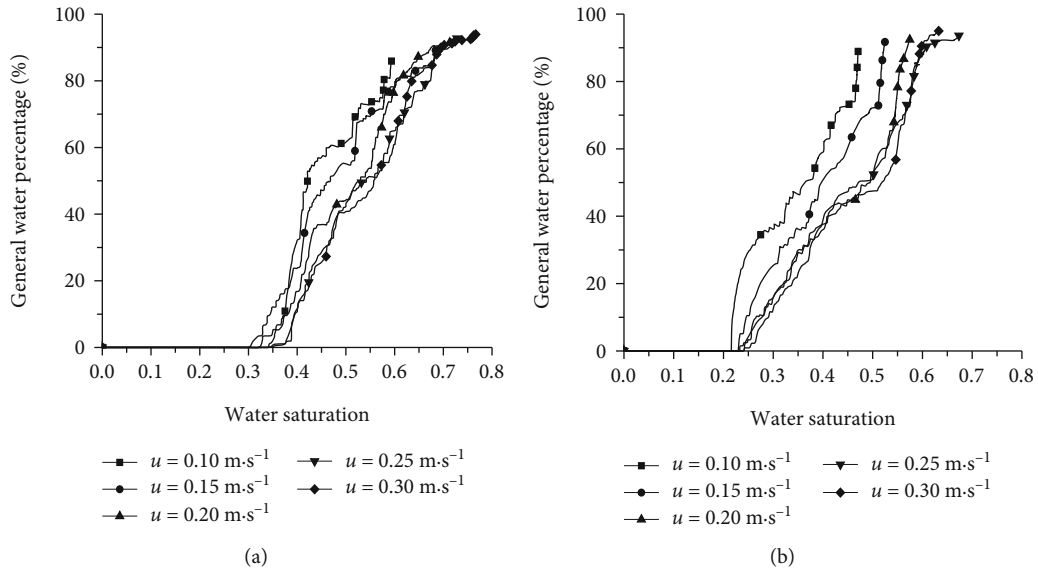


FIGURE 2: Water flooding curve at different injection velocity: (a) contact angle $\theta = 25^\circ$; (b) contact angle $\theta = 165^\circ$.

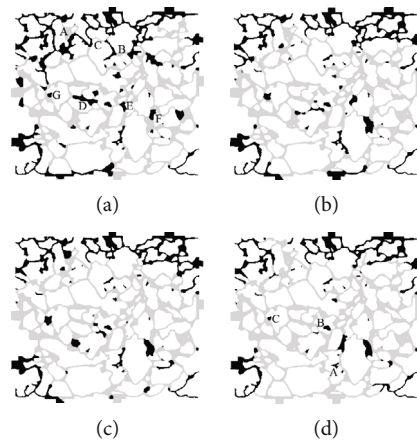


FIGURE 3: Final oil-water distribution at different water injection rates under water-wet conditions: (a) $0.10 \text{ m}\cdot\text{s}^{-1}$; (b) $0.15 \text{ m}\cdot\text{s}^{-1}$; (c) $0.20 \text{ m}\cdot\text{s}^{-1}$; (d) $0.25 \text{ m}\cdot\text{s}^{-1}$.

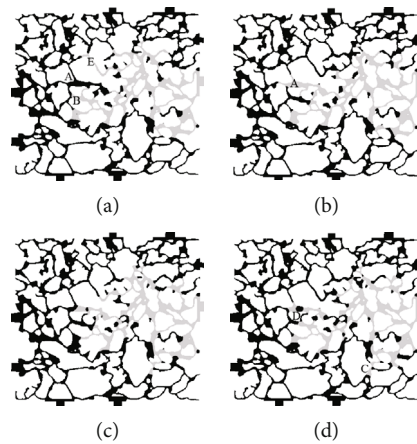


FIGURE 4: Oil distribution with same injection volume with different injection velocity under the water-wet condition (contact angle $\theta = 25^\circ$): (a) $0.10 \text{ m}\cdot\text{s}^{-1}$; (b) $0.15 \text{ m}\cdot\text{s}^{-1}$; (c) $0.20 \text{ m}\cdot\text{s}^{-1}$; (d) $0.25 \text{ m}\cdot\text{s}^{-1}$.

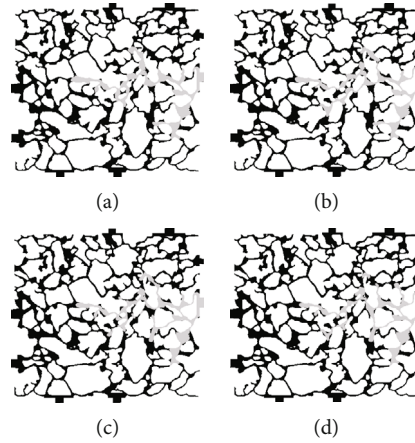


FIGURE 5: Oil distribution with same injection volume with different injection velocity under the oil-wet condition (contact angle $\theta = 165^\circ$): (a) $0.10 \text{ m}\cdot\text{s}^{-1}$; (b) $0.15 \text{ m}\cdot\text{s}^{-1}$; (c) $0.20 \text{ m}\cdot\text{s}^{-1}$; (d) $0.25 \text{ m}\cdot\text{s}^{-1}$.

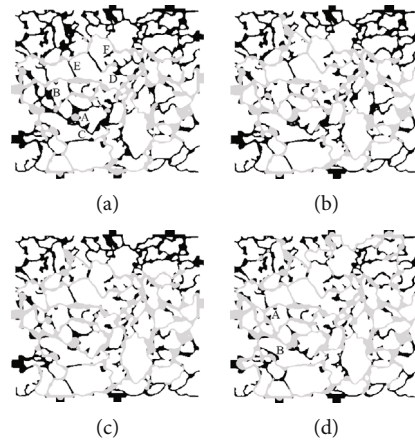


FIGURE 6: Final oil-water distribution at different water injection rates under oil-wet conditions: (a) $0.10 \text{ m}\cdot\text{s}^{-1}$; (b) $0.15 \text{ m}\cdot\text{s}^{-1}$; (c) $0.20 \text{ m}\cdot\text{s}^{-1}$; (d) $0.25 \text{ m}\cdot\text{s}^{-1}$.

example, the residual film-like oil at point B in Figure 6(d) is significantly higher than that at low speed (Figures 6(a) and 6(b)). There is little difference between the residual oil at the blind end at high injection velocity and low injection velocity.

4.2. Influence of Wall Wettability on Water Flooding Process.

In order to study the effect of wall wettability on the water flooding process, five different wettability were set under a certain same injection condition in this paper. Cases (2, 7, 12, 17, 22), (3, 8, 13, 18, 23), (4, 9, 14, 19, 24), and (5, 10, 15, 20, 25), five groups of examples, were used to calculate the water flooding process with different wettability under the same injection speed.

4.2.1. Water Flooding Curve. Figure 7 is the water content curve under different wettability conditions; Figure 7(a) is the water flooding curve when the injection velocity $u = 0.10 \text{ m}\cdot\text{s}^{-1}$, the contact angle θ is 25° , 45° , 90° , 125° , and 165° ; Figure 7(b) gives the water flooding curve of five different contact angles when the velocity $u = 0.30 \text{ m}\cdot\text{s}^{-1}$. It can

be seen from both figures that under the same velocity conditions, the final water saturation when the core wall is oil-wet is lower than that in the water-wet state; the water breakthrough time at the outlet is quite different. In Figure 7, there are great differences in the water saturation at the time of water breakthrough under different wettability, that is to say, the wettability has a great influence on the water saturation of the core at water breakthrough. Wettability has a great influence on the duration of anhydrous oil recovery period. In Figure 7(a), the recovery rate is the highest under the condition of weak water-wet, and a large number of previous experimental results also show that the oil displacement efficiency of weak water-wet cases is higher than that of strong water-wet cases.

4.2.2. Oil-Water Distribution with Same Injection Volume under Different Wettability Conditions. Figure 8 shows the distribution of oil and water before water breakthrough with different wettability at the same water injection velocity ($0.10 \text{ m}\cdot\text{s}^{-1}$) and the same water injection volume, (a) contact angle $\theta = 25^\circ$; (b) contact angle $\theta = 45^\circ$; (c) contact angle

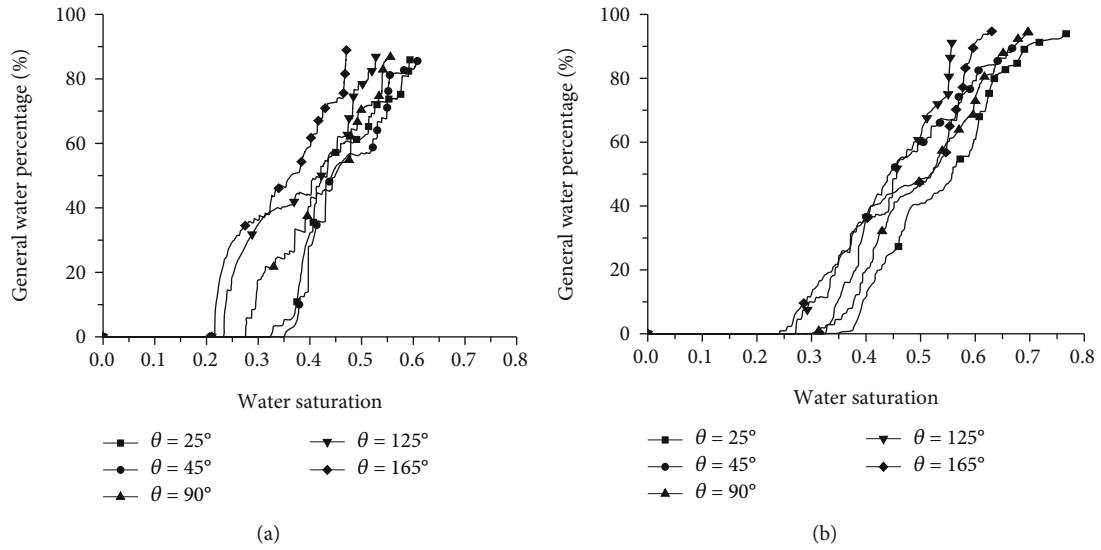


FIGURE 7: Water flooding curve under different wettability at the same injection velocity: (a) $u = 0.10 \text{ m} \cdot \text{s}^{-1}$; (b) $u = 0.30 \text{ m} \cdot \text{s}^{-1}$.

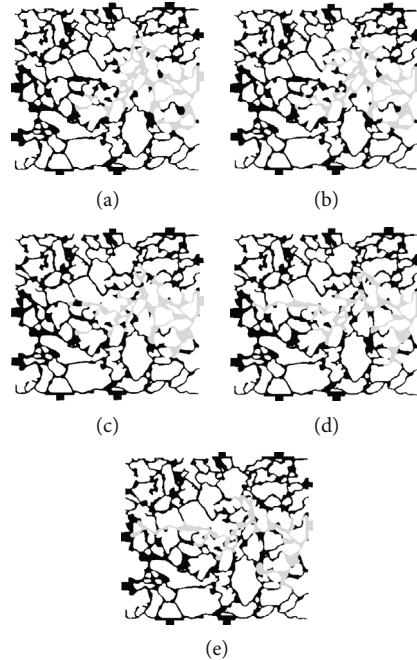


FIGURE 8: Oil-water distribution with same injection volume under different wettability conditions: (a) $\theta = 25^\circ$; (b) $\theta = 45^\circ$; (c) $\theta = 90^\circ$; (d) $\theta = 125^\circ$; (e) $\theta = 165^\circ$.

$\theta = 90^\circ$; (d) contact angle $\theta = 125^\circ$; (e) contact angle $\theta = 165^\circ$. In the figure, black represents oil, and gray represents water. It can be seen from the figure that on the whole, the water moves along the direction of the connection line between the inlet and outlet, and there is an obvious fingering phenomenon. When the contact angle is larger, the viscous fingering is more obvious, and viscous fingering in oil-wet cases is more obvious than that of water-wet cases. The capillary fingering perpendicular to the flow direction is much larger in water-wet conditions than in oil-wet conditions, making it easier for water to migrate in the direction

perpendicular to the main flow in a water-wet environment. These findings are consistent with previous experimental observations in two-dimensional micromodels [27, 28] and three-dimensional rock [26, 29]. The displacement patterns are widely recognized to exhibit viscous fingering, capillary fingering, and stable displacement, which are controlled by the competition between the viscous and capillary forces. It can be seen from Figures 8(a)–8(c) that some water leaves the displacement front, but this phenomenon is not seen in the displacement front in Figures 8(d)–8(e), which is also caused by capillary action.

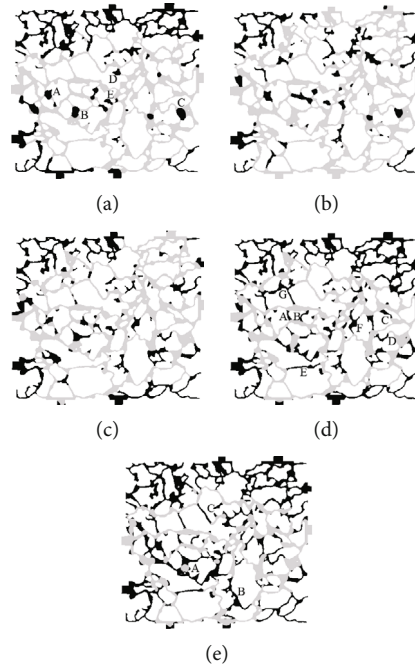


FIGURE 9: Final oil-water distribution under different wettability conditions: (a) $\theta = 25^\circ$; (b) $\theta = 45^\circ$; (c) $\theta = 90^\circ$; (d) $\theta = 125^\circ$; (e) $\theta = 165^\circ$.

4.2.3. Final State Oil-Water Distribution under Different Wettability Conditions. Figure 9 shows the distribution of the final remaining oil under different wettability: (a) contact angle $\theta = 25^\circ$; (b) contact angle $\theta = 45^\circ$; (c) contact angle $\theta = 90^\circ$; (d) contact angle $\theta = 125^\circ$; (e) contact angle $\theta = 165^\circ$. In general, the recovery rate under water-wet conditions is higher than that under oil-wet conditions. The degree of sweep perpendicular to the flow direction is more in water-wet cases and that in oil-wet cases. Under water-wet conditions, the oil in the swept area was completely recovered, and the residual oil in the swept area mainly existed in pores (A, B, C in Figure 9(a)) and the blind end (Figure 9(a) positions D, E). In an oil-wet environment, due to the hindering effect of interfacial tension on water, water displaces oil in large pores, and the residual oil in the swept area mainly exists in small pores (points A B C D E in Figure 9(d)) and in the blind end (Figure 9(e), point C) and in the large pores surrounded by small pore channels (Figure 9(d), point FG).

5. Conclusions

In this paper, a numerical simulation of oil-water two-phase flow in a real sandstone porous medium is performed using the interFoam solver in the open source fluid mechanics software OpenFOAM. The influence of different injection velocities and different wall wettability on oil-water movement and residual oil distribution during water flooding was studied, and the following conclusions were obtained:

- (1) The larger the injection rate, the larger the swept area, the higher the recovery factor, and the less residual oil in the swept area. Under water-wet conditions, the

higher the velocity, the easier it is to displace the oil in the large pores, and the lower the velocity, the easier it is to displace the oil in the small pores

- (2) Wettability affects how water is swept up and where the remaining oil appears. When the rock is water-wet, the sweep perpendicular to the flow direction is stronger than the oil-wet cases due to capillary fingering; when the rock is oil-wet, the viscous fingering dominates, resulting in the fingering in the flow direction being more in the oil-wet cases than that in water-wet cases. The residual oil in the swept area of water-wet rocks mainly appears in large pores and blind ends, while the residual oil in the swept area of oil-wet rocks mainly appears in pores surrounded by small pores, slender throats between pores, blind ends, and pore walls with larger pore-throat ratio
- (3) Wettability affects single-channel recovery rate efficiency. With the increase of the contact angle, the recovery rate decreases gradually, but the oil displacement efficiency is the highest in the weak water-wet state. The oil displacement efficiency of the single channel in the water-wet condition is obviously higher than that in the oil-wet condition

Data Availability

The experimental data used to support the findings of this study are included within the manuscript.

Conflicts of Interest

The authors declared that there is no conflict of interest.

Acknowledgments

This research was funded by Key R&D Program of Ningxia Hui Autonomous Region, grant number: 2021BEE03009.

References

- [1] Y. Wang, Y. Liu, and Q. Deng, "Current situation and development strategy of the extra high water cut stage of continental facies sandstone oil fields in China," *Journal of Northeast Petroleum University*, vol. 38, no. 1, pp. 1–9, 2014.
- [2] C. Zou and L. Yu, "A quantization relationship between water cut and degree of reserve recovery for water-flooding sandstone reservoirs in China," *Acta Petrolei Sinica*, vol. 33, no. 2, pp. 288–292, 2012.
- [3] D. Ren, L. Ma, D. Liu, J. Tao, X. Liu, and R. Zhang, "Control mechanism and parameter simulation of oil-water properties on spontaneous imbibition efficiency of tight sandstone reservoir," *Frontiers in Physics*, vol. 10, no. 10, article 829763, 2022.
- [4] B. Rostami and G. L. Morini, "Experimental characterization of a micro cross-junction as generator of Newtonian and non-Newtonian droplets in silicone oil flow at low capillary numbers," *Experimental Thermal and Fluid Science*, vol. 103, pp. 191–200, 2019.
- [5] T. Akai, A. M. Alhammad, M. J. Blunt, and B. Bijeljic, "Modeling oil recovery in mixed-wet rocks: pore-scale comparison between experiment and simulation," *Transport in Porous Media*, vol. 127, no. 2, pp. 393–414, 2019.
- [6] Y. Tang, A. J. Valocchi, C. J. Werth, and H. Liu, "An improved pore-scale biofilm model and comparison with a microfluidic flow cell experiment," *Water Resources Research*, vol. 49, no. 12, pp. 8370–8382, 2013.
- [7] Z. Li, Z. Gu, R. Li et al., "A geometrical criterion for the dynamic snap-off event of a non-wetting droplet in a rectangular pore-throat microchannel," *Physics of Fluids*, vol. 34, no. 4, article 042014, 2022.
- [8] Z. Li, L. Gu, R. Li et al., "Investigation on droplet dynamic snap-off process in a short, abrupt constriction," *Chemical Engineering Science*, vol. 235, article 116496, 2021.
- [9] G. Sheng, Y. Su, and W. Wang, "A new fractal approach for describing induced-fracture porosity/permeability/compressibility in stimulated unconventional reservoirs," *Journal of Petroleum Science and Engineering*, vol. 179, pp. 855–866, 2019.
- [10] T. Ning, M. Xi, B. Hu, L. Wang, C. Huang, and J. Su, "Effect of viscosity action and capillarity on pore-scale oil–water flowing behaviors in a low-permeability sandstone waterflood," *Energies*, vol. 14, no. 24, p. 8200, 2021.
- [11] X. Liu, L. Wang, J. Wang, and J. Su, "Pore-scale simulation of particle flooding for enhancing oil recovery," *Energies*, vol. 14, no. 8, p. 2305, 2021.
- [12] J. Su, G. Chai, L. Wang et al., "Direct numerical simulation of pore scale particle-water-oil transport in porous media," *Journal of Petroleum Science and Engineering*, vol. 180, pp. 159–175, 2019.
- [13] J. Su, G. Chai, L. Wang et al., "Direct numerical simulation of particle pore-scale transport through three-dimensional porous media with arbitrarily polyhedral mesh," *Powder Technology*, vol. 367, pp. 576–596, 2020.
- [14] D. Ren, H. Zhang, Z. Wang, B. Ge, D. Liu, and R. Zhang, "Experimental study on microscale simulation of oil accumulation in sandstone reservoir," *Frontiers in Physics*, vol. 10, no. 10, article 841989, 2022.
- [15] J. J. Li, H. Q. Jiang, J. R. Hou, and S. L. Wang, "The effects of oil displacement efficiency and conformance efficiency on viscosity of asp flooding in a heterogeneous reservoir," *Liquid Fuels Technology*, vol. 32, no. 7, pp. 830–839, 2014.
- [16] C. Xie, W. Lei, M. T. Balhoff, M. Wang, and S. Chen, "Self-adaptive preferential flow control using displacing fluid with dispersed polymers in heterogeneous porous media," *Journal of Fluid Mechanics*, vol. 906, p. A10, 2021.
- [17] G. Tryggvason, B. Bunner, A. Esmaeeli et al., "A front-tracking method for the computations of multiphase flow," *Journal of Computational Physics*, vol. 169, no. 2, pp. 708–759, 2001.
- [18] E. Olsson and G. Kreiss, "A conservative level set method for two phase flow," *Journal of Computational Physics*, vol. 210, no. 1, pp. 225–246, 2005.
- [19] C. W. Hirt and B. D. Nichols, "Volume of fluid (VOF) method for the dynamics of free boundaries," *Journal of Computational Physics*, vol. 39, no. 1, pp. 201–225, 1981.
- [20] A. Q. Raeini, M. J. Blunt, and B. Bijeljic, "Modelling two-phase flow in porous media at the pore scale using the volume-of-fluid method," *Journal of Computational Physics*, vol. 231, no. 17, pp. 5653–5668, 2012.
- [21] Y. Yang, S. Cai, J. Yao et al., "Pore-scale simulation of remaining oil distribution in 3D porous media affected by wettability and capillarity based on volume of fluid method," *International Journal of Multiphase Flow*, vol. 143, article 103746, 2021.
- [22] <http://www.openfoam.com>.
- [23] S. S. Deshpande, L. Anumolu, and M. F. Trujillo, "Evaluating the performance of the two-phase flow solver interFoam," *Computational Science & Discovery*, vol. 5, no. 1, article 014016, 2012.
- [24] G. R. Guédon, F. Inzoli, M. Riva, and A. Guadagnini, "Pore-scale velocities in three-dimensional porous materials with trapped immiscible fluid," *Physical Review E*, vol. 100, no. 4, article 043101, 2019.
- [25] H. Aslannejad, S. V. Loginov, B. van der Hoek, E. M. Schoonderwoerd, H. C. Gerritsen, and S. M. Hassanizadeh, "Liquid droplet imbibition into a thin coating layer: direct pore-scale modeling and experimental observations," *Progress in Organic Coatings*, vol. 151, article ???, 2021.
- [26] Y. Hu, A. Patmonoaji, C. Zhang, and T. Suekane, "Experimental study on the displacement patterns and the phase diagram of immiscible fluid displacement in three-dimensional porous media," *Advances in Water Resources*, vol. 140, article 103584, 2020.
- [27] R. Lenormand, E. Touboul, and C. Zarcone, "Numerical models and experiments on immiscible displacements in porous media," *Journal of Fluid Mechanics*, vol. 189, pp. 165–187, 1988.
- [28] C. Zhang, M. Oostrom, T. W. Wietsma, J. W. Grate, and M. G. Warner, "Influence of viscous and capillary forces on immiscible fluid displacement: pore-scale experimental study in a water-wet micromodel demonstrating viscous and capillary fingering," *Energy & Fuels*, vol. 25, no. 8, pp. 3493–3505, 2011.
- [29] D. Ren, X. Wang, Z. Kou et al., "Feasibility evaluation of CO₂ EOR and storage in tight oil reservoirs: a demonstration project in the Ordos Basin," *Fuel*, vol. 331, article 125652, 2023.